ADVANCED FUNCTIONAL MATERIALS
www.afm-journal.de

A Skin-Mountable Hyperthermia Patch Based on Metal Nanofiber Network with High Transparency and Low Resistivity toward Subcutaneous Tumor Treatment

Qi Wang, Hongwei Sheng, Yurong Lv, Jie Liang, Yan Liu, Na Li, Erqing Xie, Qing Su, Faheem Ershad, Wei Lan, Jing Wang,* and Cunjiang Yu**

A wearable hyperthermia device that allows for tumor treatment without interfering with daily activities is of clinical and social significance. However, the wide adaptation of local hyperthermia from such wearable devices in clinical practice has been hindered mainly due to several critical challenges in existing hyperthermia devices, such as the contradiction of high electrical conductivity and high optical transparency of the device while in a thin, deformable format. Here a soft, skin-mountable, hyperthermia patch (HTP) is reported with unusual optical and electrical characteristics based on unidirectional silver nanofibers (AgNFs) network with low-voltage operation and uniform heating even under mechanical deformation. The patch presents both high electrical conductivity and highly optical transparency simultaneously thus allowing real time inspection of the subcutaneous tumor treatment and skin response during the treatment. The unidirectional nature of the AgNFs network renders the key features of high optical transparency, low electrical resistivity, excellent electrothermal performances, and mechanical deformability. Effective treatment of subcutaneous tumors in mice is demonstrated with the skin worn HTP while the skin response is visually tracked. Systematic studies reveal the physiological mechanisms of Notch signaling in inducing tumor cell apoptosis.

1. Introduction

Hyperthermia, which causes hypoxia and acidosis in tumor tissues, resulting in autophagy of tumor cells without damaging normal tissues,[1] has many advantages in non-invasiveness and minimal side effects compared with other common treatment methods, such as surgery,[2–3] chemotherapy and radiotherapy,[4] biological therapy,[5] and phototherapy,[6] and is considered to be one of the promising and auxiliary means to cure tumors. In particular, a hyperthermia device that is based on the Joule heating mechanism and can be worn on human bodies, thus allowing for treatment without interfering in daily activities, is of clinical and social significance. However, the wide adaptation of local hyperthermia delivered by wearable Joule heating devices in clinical practice has been hindered mainly owing to several key drawbacks in the existing hyperthermia devices.[7] Conventional heat wraps and packs for hyperthermia are relatively bulky and heavy, which make it difficult for them to interface closely with human skin, to effectively deliver thermal energy, and to control the local temperature.[8–9] In addition, they are optically opaque, which prevents real-time, continuous tracking of the treatment status, and likely causes skin burn and sensory impairment in the treatment area.[10] Ideally, a wearable hyperthermia device should have features of i) mechanical softness, thin form factor, and ability to seamlessly contact with skin, ii) spatially uniform temperature distribution, fast response, and temperature controllability, iii) electrical safety with low-voltage operation, and iv) high optical transparency to allow visual inspection and to prevent any overheating or skin burn.

Q. Wang, H. Sheng, J. Liang, E. Xie, Q. Su, W. Lan
School of Physical Science and Technology
Lanzhou University
Lanzhou, Gansu 730000, China
E-mail: lanw@lzu.edu.cn

Y. Lv, Y. Liu, N. Li, J. Wang
School of Stomatology
Lanzhou University
Lanzhou, Gansu 730000, China
E-mail: wangjing@lzu.edu.cn, lzukqwj@126.com

The ORCID identification number(s) for the author(s) of this article can be found under https://doi.org/10.1002/adfm.202111228.

F. Ershad, C. Yu
Department of Biomedical Engineering
University of Houston
Houston, TX 77204, USA
E-mail: cyu13@central.uh.edu

F. Ershad, C. Yu
Departments of Mechanical Engineering and Electrical and Computer Engineering
Texas Center for Superconductivity
University of Houston
Houston, TX 77204, USA

DOI: 10.1002/adfm.202111228

 © 2022 Wiley-VCH GmbH

Recently, there has been lots of advancement in developing mechanically soft Joule heating materials and devices for different applications.[11–15] Nevertheless, they could not be readily employed as ideal hyperthermia treatment devices due to several intrinsic challenges. In general, it is generally challenging to achieve high electrical conductivity and high optical transparency simultaneously in conductors in various formats such as thin films, networked materials, and composites.[7,16–17] For conventional transparent conductors, high voltage is required to achieve effective Joule power thus leading to unsafe operation when worn.[18] In addition, large mechanical deformations associated with wearing and ambulatory movement usually results in cracks or flaws in conductors, which result in local hot spots and/or non-uniform heating.[19] Consequently, developing mechanically soft, transparent hyperthermia device with outstanding electrothermal performances are highly desirable.

Here we present a soft, skin-mountable, hyperthermia patch (HTP) with based on unidirectional silver nanofibers (AgNFs) network, which have unusual optical and electrical performances by achieving both low electrical resistivity and high optical transparency over a broad spectrum simultaneously. The directionality of the AgNFs network is one of the keys to its electrothermal and mechanical characteristics. Experiments and finite element analyses provide a quantitative understanding of the AgNFs network's electrothermal characteristics and thermal profiles over time. To validate the conformal attachment and function of the HTP, it is laminated onto various human joints and on mice with subcutaneous tumors for hyperthermia treatment. The optical transparency of HTP is critical for patients with skin sensation loss partially or fully to monitor abnormal skin irritation in real-time, thereby regulating the applied voltage to avoid burns. Its hyperthermia treatment capabilities are illustrated by effectively curing subcutaneous tumors in nude mice, where the tumor growth was dramatically suppressed after mild-thermic (42°C) treatment while operating at an ultra-low voltage (0.7 V). Systematic analysis on the tumor cells further indicates that hyperthermia from such an HTP can significantly inhibit the growth of subcutaneous tumors by inducing cell apoptosis. This mild-thermic therapy strategy based on Joule heating offers a viable clinical venue for treating joint injuries and superficial tumors.

2. Results and Discussion

2.1. Transparent Hyperthermia Patch

As schematically shown in **Figure 1**a, the designed soft, transparent HTP has three functional layers, including the metalized AgNFs network as a heating electrode, middle polymer supporting layer, and an external packaging layer (polydimethylsiloxane, PDMS). The supporting layer consists of the top polyvinyl pyrrolidone (PVP) and bottom poly(vinyl alcohol) (PVA) polymers. The combination of the functional and supporting layers can resist tension during excessive bending and prevent conductive fibers from breaking, since the Young's modulus for PVA (≈2.13 GPa) is much higher than that of PDMS (≈145 kPa).[20–21] The fabrication process of the HTPs is illustrated in Figure S1 (Supporting Information) and is further described in detail in the Methods section. Specifically, large-scale poly(vinyl alcohol) (PVA) nanofiber networks with different web structures were prepared by adjusting the electrospinning parameters (Figure S2, Supporting Information). Next, a thin layer (thickness ≈60 nm) of Ag was deposited on the surface of PVA nanofibers through magnetron sputtering at room temperature (Figure S3a, Supporting Information). The metalized AgNFs network is therefore formed based on such PVA-Ag core–shell nanofibers with excellent electrical conductivity. The resulting metalized AgNFs have an average diameter of ≈700 nm and smooth surface morphology (Figure S3b,c, Supporting Information), benefiting from the large kinetic energy and distribution uniformity of the sputtered Ag films, and low surface roughness of PVA fibers obtained through electrospinning. The corresponding energy-dispersive X-ray spectrometry (EDX) elemental mappings further confirmed the uniform distribution of metallic Ag on the overall surface of the nanofibers, consistent with X-ray diffraction (XRD) analysis (Figure S3d, Supporting Information). In order to avoid the oxidation of Ag due to long-term exposure in air and ensure mechanical compliance with the skin, the metalized AgNFs network was externally encapsulated with a soft PDMS layer. Storing the encapsulated HTPs in a high-temperature environment (80.0 °C) did not affect their resistances over a couple of months and their functions were retained (Figure S4, Supporting Information).

The working temperature of the HTP is determined by two processes:[14] one is the inflow and storage of the electrical energy, and the other is the outflow and releasing of the thermal energy through heat transfer to the surrounding air. The heat losses can be divided into three types: heat conduction to the substrates, heat convection to the surrounding air, and thermal radiation (Figure S5, Supporting Information). The first thermal conduction is used for hyperthermia. Regarding the thermal radiation, its contribution to the total heat loss of the HTPs can be neglected, considering the low temperature of the HTPs.[22] Apart from the uncontrollable external factors and inherent properties, the key to achieving high performance hinges on the preparation of the electrode. By optimizing the direction and arrangement of the fibers, both low resistance and high optical transmittance are achieved in our HTP. At the same transmittance, the unidirectional AgNFs network based HTP can achieve the required temperature while operating at an ultra-low voltage, due to its low resistance along the current direction. In addition, an HTP with features of thin structure (Figure 1b) and good mechanical softness (Figure 1c) can be conveniently and conformally attached to various locations on the body for efficient heat transfer. The thickness of the HTP is less than 200 μm, and its overall size can be controlled as required (Figure S6, Supporting Information). Based on the obtained experimental results, we simulated the differences in temperature distribution of the skin attachable HTP after heat conduction into the subcutaneous tissue via finite element analysis (FEA), as shown in Figure 1d. The simulation results indicate that no excessive heat is applied to the subcutaneous tissues. Figure 1e presents the apoptotic process of the subcutaneous tumor tissue treated by the HTPs. The Joule heat generated by

© 2022 Wiley-VCH GmbH

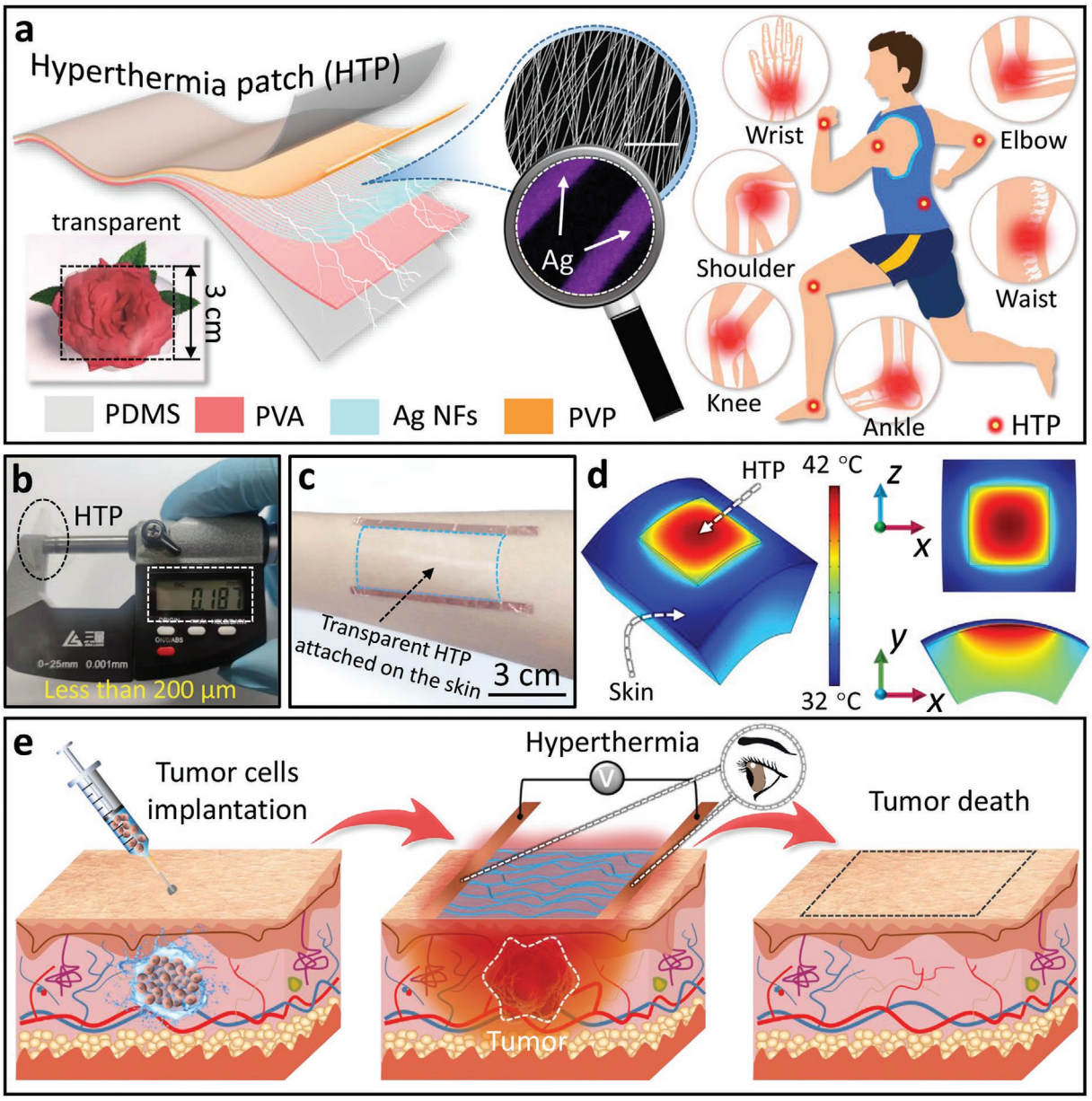

Figure 1. A thin, soft, transparent, and high-performance HTP based on AgNFs network for tumor hyperthermia. a) Schematic illustration of the HTP including the metalized AgNFs network heating layer, PVA and PVP supporting layer, and PDMS elastomer encapsulation layers. The insets are an SEM image and EDX elemental mapping of the unidirectional AgNFs network. Scale bar: 50 μm. An application scenario of the HTP that can be conveniently and conformal attached to various joints in the human body for hyperthermia is shown on the right. b) Photograph of the encapsulated HTP with less than 200 μm thickness. c) Soft and transparent display of HTP attached on the skin, and d) the corresponding temperature distributions of HTP under a heating state simulated using finite element analysis (FEA). e) Apoptotic process of subcutaneous tumors induced by hyperthermia.

the HTP can be effectively transmitted through the epidermis to the tumor site. Our HTPs exhibit combined advantages due to their broadband optical transparency ranging from the ultraviolet (UV) to infrared (IR) range. It is noted that the size of the HTP can be customized based upon the targeted treatment area. In addition, temperature monitoring and thus control, and the adjustment of the operation time can prevent overheating and skin burns thus to eliminate potential tissue damage. It is also noted that the HTPs can be reused after UV sterilization.

2.2. Electrothermal Properties of HTPs

Central criteria for the HTP are mechanical softness, high optical transparency, rapid-thermal response, uniform temperature distribution, and low voltage operation. Based on the Joule heating effect, when a bias voltage (U) is applied to uniform conductive materials with a sheet resistance (R_s), the Joule heat power (P) is equal to U^2/R_s. In general, the realization of low resistivity and high transparency is a challenge due to the contradiction between these two, where low resistivity is usually

© 2022 Wiley-VCH GmbH

accompanied by low transparency due to the percolation nature of conductive networks,[23–26] as shown in Figure S7 (Supporting Information). Here, the metalized AgNFs were selected as the transparent conductor because they form a bridge that is a complete conducting path from one side of the electrode to the other, which is not affected by electrical percolation. The preparation of the metalized AgNFs is as follows.

The electrospinning technique was employed to produce continuous fiber structures with controllable diameters on the order hundreds of nanometers. To achieve an ideal transparent HTP, direction and density of the AgNFs could be optimized by altering the custom-made metal collector frames and electrospinning time. As shown in **Figure 2**a, large-scale AgNFs network-based HTPs with two typical types (including unidirectional and omnidirectional) were prepared, and their heating properties were also evaluated. The counted results of the mean deviation angles from the orientation direction show that unidirectional AgNFs network has the highest alignment with the lowest mean deviation angle of 10.54°, in accordance with the morphological results. Next, we compared the time-dependent temperature profiles (Figure 2b) of the two kinds of HTPs with the same transmittance (Figure S8, Supporting Information). In contrast, when the same voltage (1.2 V) was supplied, unidirectional AgNFs network-based HTPs exhibit a higher saturation temperature (96.7 °C) owing to more efficient conductive pathways along the current direction. This is because the

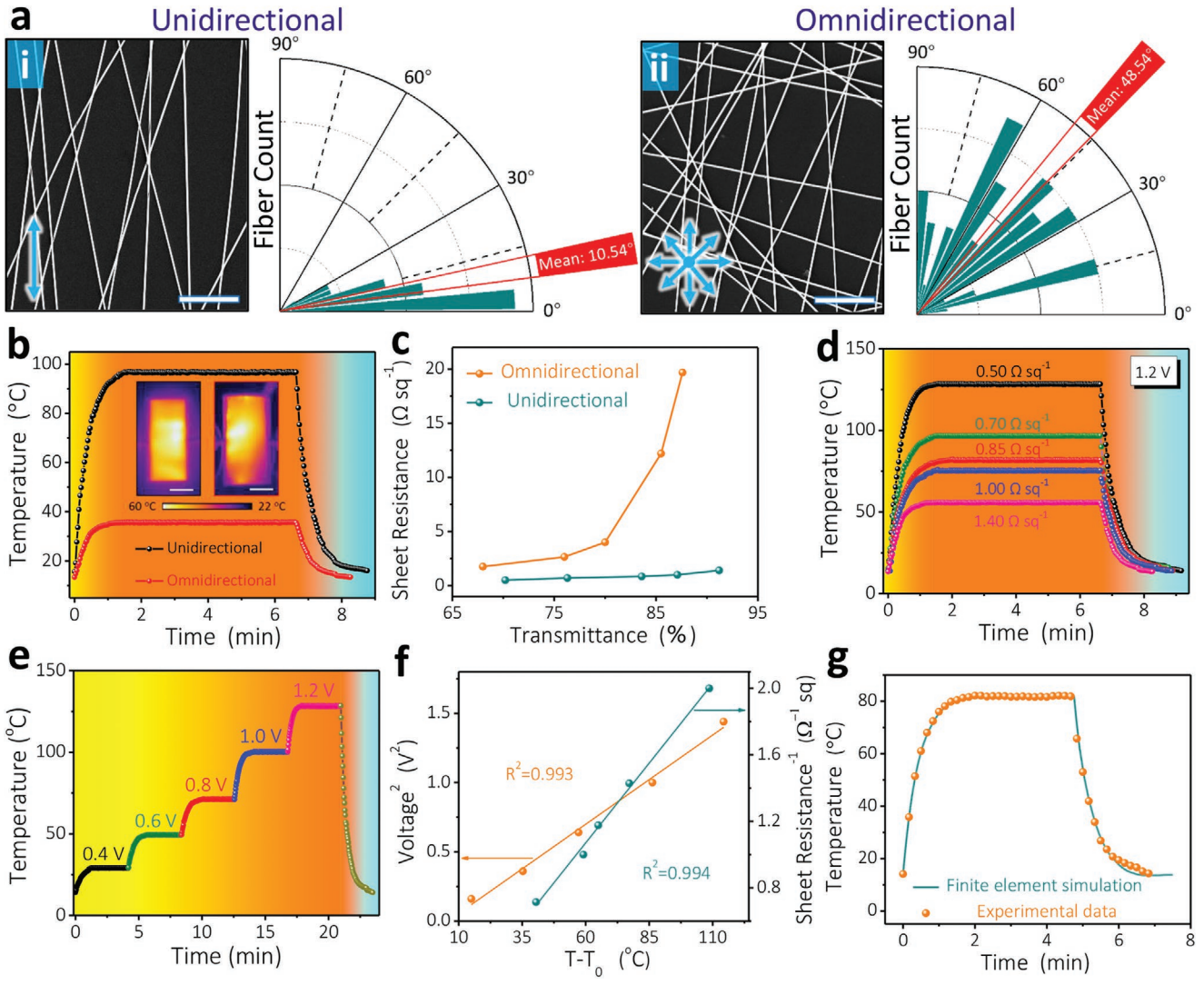

Figure 2. Effect of fiber direction on electrothermal properties. a) SEM images of the unidirectional and omnidirectional AgNFs networks, and corresponding mean deviation angles from the orientation direction. Scale bars: 20 µm. b) Time-varying surface temperature of the HTPs with two types at the same transmittance. Insets are infrared (IR) images of two types of HTP. Scale bars: 2 cm. and c) their sheet resistance (R_s) changes at different transmittances (at 550 nm). The calculated sheet resistance here is along the electrical current direction. d) The time-varying surface temperature of the unidirectional AgNFs network based HTP with different R_s at 1.2 V. e) Tailored surface temperature of the unidirectional AgNFs network based HTP at applied gradient voltages for a R_s of 0.5 Ω sq^{-1}. f) The square of the voltage (U^2) and the reciprocal of R_s plotted as a function of temperature differences (ΔT). The solid line is obtained by fitting the points using Equation (2). g) Measured (dots) and simulated (solid line) surface temperature as a function of time for the HTP with a R_s of 0.85 Ω sq^{-1} at 1.2 V.

© 2022 Wiley-VCH GmbH

omnidirectional AgNFs network is randomly distributed, and the enumourous nodes between the fibers lead to higher contact resistance. Instead, unidirectional AgNFs can minimize the number of nodes between 1D metallic geometries, which can greatly reduce the sheet resistance (R_s) while maintaining large open spaces in the networks to achieve high transmittance. In addition, the IR images (inset of Figure 2b) of the patch with the unidirectional AgNFs network show better thermal uniformity after heating to a thermally stable state, compared with the omnidirectional AgNFs network. This might be due to weak interconnections in omnidirectional networks between AgNFs and invalid conductive paths on the edges and corners (Figure S9, Supporting Information), resulting in local hot/dark spots, and uneven heat distribution. By altering the electrospinning duration, the two types of HTPs with various transmittances were also prepared (Figures S10–S12, Supporting Information). Their transmittance (at 550 nm) as a function of the R_s along the current direction is presented in Figure 2c. The test method for the R_s is illustrated in Figure S13 (Supporting Information). Unlike the omnidirectional AgNFs network, the R_s of the unidirectional AgNFs network almost remains the same as the transmittance increases. This is because the transmittance mainly depends on the empty areas between AgNFs. When the light passes through the films, the nodes of AgNFs block the light, leading to lower transparency (Figure S14, Supporting Information). The number of nodes in the unidirectional AgNFs network is obviously lower than that of the omnidirectional AgNFs network. As such, the unidirectional AgNFs network outperformed the omnidirectional AgNFs network in both the R_s and transmittance. At a given transmittance (91.2%), the R_s of the unidirectional AgNFs network reaches 1.40 Ω sq^{-1}. Figure 2d presents the thermal response behavior of the unidirectional AgNFs network based HTPs with different resistances at a constant voltage of 1.2 V. The steady-state temperature decreased with the growing resistance at a given input voltage. The HTP with a R_s of 0.50 Ω sq^{-1} can reach the maximum steady-state temperature of 128.2 °C, which is reduced to 55.8 °C for the HTP having an R_s of 1.40 Ω sq^{-1}. Figure 2e shows the temperature-time profiles of the HTP with stepwise voltages from 0.4 to 1.2 V. The tailored surface temperature of the HTPs reached steady state within ≈50 s, and then the saturated temperature was maintained at each step. It is worth noting that the saturated temperature at each bias is consistent with the results shown in Figure S15a (Supporting Information). The experimental results (Figure 2g) are well-matched with the FEA simulation results, revealing that the prepared HTP is an ideal Joule heat generator. As shown in Figure S16 (Supporting Information), the HTPs with different R_s show the volt-ampere characteristic curve of a purely resistive device. To sum up, it can be observed that the unidirectional AgNFs network based HTPs exhibit excellent electrothermal characteristics, including a wide temperature range (30.0–128.2 °C), low driving voltage (0.4–1.2 V), rapid thermal response (<50 s), good thermal uniformity, and excellent operational stability to bear various harsh conditions, which generally exceed that of currently reported devices (see detailed data in Table S1, Supporting Information).[7,12,16,19,27–38]

Furthermore, the fitted steady-state temperature–input power (T_s–P) curves are shown in Figure S15b (Supporting Information), showing the heating efficiency of the HTPs. The value of the T_s and P correspond to those shown in Figure 2e. When the heat input and loss reach a dynamic balance, the steady-state temperature of HTPs can be achieved as follows:

$$T_s = T_0 + \frac{P}{Ah} \tag{1}$$

where T_0 is the environment temperature, h refers to the total sum of the heat transfer coefficient, and A is the surface area. The experimental dependence between T_s and P was fitted very well by using Equation (1), indicating that T_s increased linearly as the driving power increased. In order to better understand the resistance variation with the thermal response behavior of HTPs, the Equation (2) is also written as

$$\Delta T = \frac{U^2}{AhR_s} \tag{2}$$

where ΔT is defined as the difference between T_s and T_0. As seen from Equation (2), ΔT scales inversely with R_s, and is proportional to U^2. Figure 2f is the ΔT plotted as a function of U^2 and $1/R_s$. All measured data points were well fitted using Equation (2). Goodness of fit (R^2) is greater than 0.99, indicating that the resistance and heat dissipation area remain basically unchanged at high temperatures. All these results suggest that the unidirectional AgNFs network has great potential for transparent, heating devices with closed-loop temperature control.

2.3. Flexibility, Wearability, and Stability of HTPs

Excellent flexibility of the unidirectional AgNFs network-based HTPs was revealed in two deformation tests: i) after being clenched in the hand and then released to its natural state (**Figure 3**a) and ii) after several bending cycles. After the first deformation test, the unidirectional AgNFs network retained its original appearance without any observable creases. The second deformation test shows that the HTP remains functional when folded many times, as it can still turn on a commercial light-emitting diode (LED) (Figure S17, Supporting Information). Figure 3b shows the relative surface temperature of the HTP during repeated bending (Figure S18, Supporting Information). No structural cracks were found in the HTP and its heating stability was barely affected after bending thousands of times. The corresponding resistance variation (Figure S19, Supporting Information) of the HTPs under more severe bending conditions also confirms these results. To further check the thermal stability and repeatability of the HTPs, the voltage driving the HTP was turned on and off in quick succession (Figure S20, Supporting Information). Even after repeated heating-cooling tests at 1.2 V, the HTPs maintained stable and fast thermal response characteristics. The environmental stability was also tested by operating the HTPs under different ambient conditions. Figure 3c shows the time-dependent temperature profiles of HTPs at different ambient temperatures. The target temperature could be controlled by varying the applied voltage. For example, to achieve a suitable thermotherapy temperature (42.0 °C), the voltage applied to the HTPs was set as 0.5, 1.0, and 1.5 V at an ambient temperature of 27.6, 10.0, and –15.0 °C, respectively. Three measured data points (Figure S21, Supporting Information) were also well fitted using Equation (2).

© 2022 Wiley-VCH GmbH

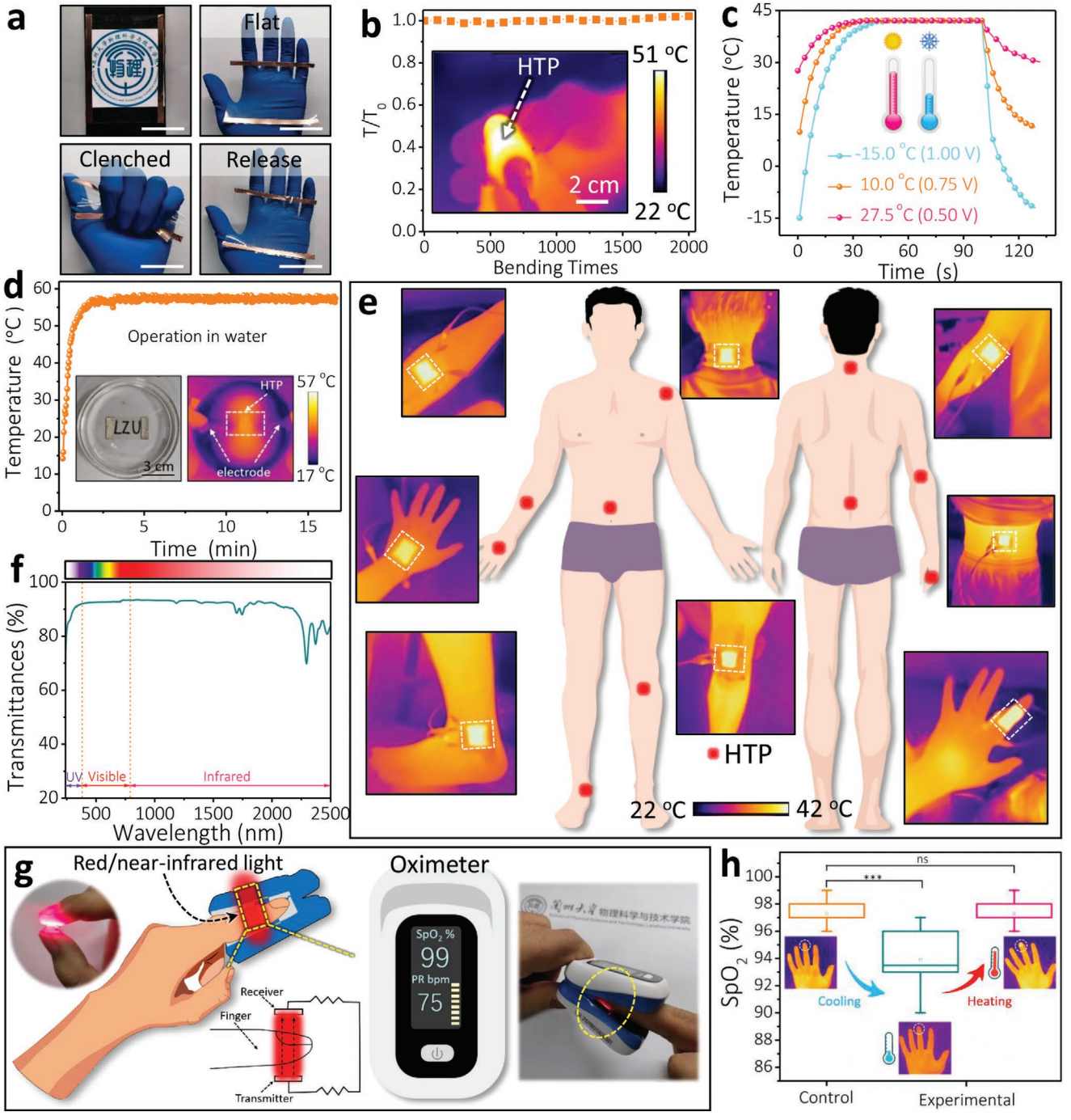

Figure 3. Operational stability of the HTP and its applications under various conditions. a) Photographs of the HTP in flat, clenched in the hand and after release conditions. Scale bars: 4 cm. b) Long-term heating stability of the HTP at a constant voltage of 0.6 V during repeated bending. Time-varying surface temperature of HTPs c) at different ambient temperatures, and d) in water (≈15 °C). The insets are the measurement setup and IR image of water heated to ≈57 °C. e) Illustration of the HTPs (size, 3 × 3 cm) mounted across the human body, with corresponding IR images of the HTPs at representative locations in insets. f) Transmittance broad spectra of the HTP. g) Finger clip based pulse oximetry with a wearable HTP. The corresponding measurement method and photo of glowing red light through living tissue with the HTP are shown in the inset. h) Statistical analysis of the measured SpO_2 from finger at ambient temperatures. n.s.: not significant. ***$p < 0.001$.

Besides, the as-prepared HTP with dimensions of 2.0 × 3.0 cm^2 was soaked in a glass Petri dish filled with deionized (DI) water and then heated at 1.5 V. The real-time temperature of DI water is also monitored, as shown in Figure 3d. The heat generated from HTP is efficiently transferred to the DI water inside, and the water temperature rises from the initial 15.0 °C to 57.0 °C after heating for 1 min. Owing to the high specific heat of water, the maximum temperature is maintained at 57.0 °C and the HTP can

© 2022 Wiley-VCH GmbH

operate steadily in water (Figure S22, Supporting Information). Taken together, the transparent HTPs based on the unidirectional AgNFs network possess good Joule heating performances, outstanding flexibility, excellent thermal stability/repeatability, and can meet different temperature requirements at an ultra-low voltage. Considering their performances, the transparent HTPs have a great potential in various biomedical applications, including heating blood bags and usage in the treatment of various types of arthritis, stiff joints, cervical spondylosis, and physical injuries.

Human joints are frequently injured in daily life, due to obesity, occupational overuse, or aging.[39–40] Joint injuries often cause various symptoms, such as pain, swelling, and dysfunction. Hyperthermia is one of the most popular physiotherapies used in orthopedics to alleviate these symptoms. Its physiological effects consist of thermal expansion of the vascular systems (increased blood flow) and their surrounding collagen tissues, thereby relieving pain and reducing joint stiffness. Figure 3e shows schematic illustrations and the corresponding IR images (Figure S23, Supporting Information) of thermotherapy with the transparent HTPs positioned at different locations on the front and back of the body. Here, thin PDMS encapsulating layers protect the internal AgNFs network in the HTPs while allowing soft, conformal contact to the skin, ensuring uniform heating and efficient heat transfer to the body. The size of the HTPs can be customized according to the thermotherapy area, and the HTP with dimensions of 3.0×3.0 cm^2 can rapidly reach 42.0 °C under an ultra-low input voltage of 0.7 V, which is desirable for wearable devices.

Owing to its high optical transparency in the visible spectrum range, the patients can see the real-time treatment effect without the need for removing the HTPs. In addition, our HTPs are also highly transparent in the near UV and IR ranges (Figure 3f). Such optical transparency potentially confers certain other advantages, such as in medical diagnostics. For instance, local hyperthermia could elevate the local temperature of a human finger to allow accurate oximetry monitoring at a low temperature[41] without compromising the red (wavelength 660 nm) and NIR (wavelength 940 nm) light transmission through the finger (Figure 3g). A portable finger clip type oximeter (Haier, YK-80C) was employed to measure the pulse oxygen saturation (SpO_2) of a human finger at a low temperature (–15 °C in a refrigerator) and high temperature (40 °C) through the heating from the HTP. The results (Figure 3h) show that the SpO_2 of the control (at an ambient temperature of 25 °C) and heating groups is close ($p > 0.05$), and it is higher than that of the cooling group ($^{***}p < 0.001$), indicating that hypothermia has a positive effect on the measurement and could allow accurate blood oxygen monitoring. The lower SpO_2 value for the finger at low temperature is mainly due to the profound vasoconstriction caused by the activation of the sympathetic nervous system.[42]

2.4. Hyperthermia of Subcutaneous Tumors

Hyperthermia is a kind of time-honored physiotherapy that has been used to treat various diseases, such as osteoarthritis,[43] cervical spondylosis,[44] and chronic ocular surface inflammation.[15] The emerging phototherapies often suffer from toxic photothermal agents that are difficult to metabolize, low photothermal conversion efficiency, and dependence on oxygen. During treatment, the local temperature at the tumor sites is maintained above 50.0 °C,[45] causing severe burns to the skin, which greatly limits the clinical application of phototherapies. In addition to the photothermal effect, hyperthermia based on the Joule heating effect has not yet been studied. Hyperthermia treatments involve applying physical energy to heat the body or part of the body, so that the temperature of the tumor tissue is raised to an effective treatment temperature, which is maintained for a certain period of time. Due to the difference in temperature tolerance between normal tissues and tumor cells, the heat treatment can cause tumor cell apoptosis without damaging normal tissues. To evaluate the in vivo therapeutic efficacy of our transparent HTPs, a subcutaneous oral cancer model was established by subcutaneously implanting pre-cultured CAL-27 cells into the dorsal side of nude mice. CAL-27 cells were selected because they are the most common oral squamous cell carcinoma with invasiveness and significant transfer risk. As illustrated in **Figure 4**a, transparent HTPs were attached conformally to the surface of the skin after tumor formation. A very low voltage (less than 1 V) was applied to trigger Joule heating, resulting in the increased temperature of the surrounding tissues. The input voltage of the HTPs can be varied to optimize the heat generation (Figure S24a, Supporting Information). Considering the biosafety issues, the appropriate hyperthermia temperature has also been explored. In general, the heat sensation of human skin is between 20.0 and 47.0 °C. If the temperature exceeds 47.0 °C, it will cause overheating and even burns that form into blisters. There are two main factors that cause burns: one is the temperature of the heat source and the other is the action time. Both factors are equally important. Too long of a local action time, even with a heat source temperature that is not high, will result in heat that slowly penetrates tissues and eventually causes burns. The comparison experiments (at 45 and 47 °C) also confirm this point. In overheating cases, we can clearly observe the abnormal state of the skin in the treated area through the transparent HTP, such as pale skin (Figure 4b) and even thermal necrosis (Figure 4c). A mild-thermic value (42.0 °C) was adopted to the following therapy protocol (Figure 4d, and Figure S25, Supporting Information). At a given temperature, adjusting the HTP area can effectively increase the average temperature of the internal tumor. An FEA simulation was performed, assuming that the tumor is a sphere with a diameter of 6 mm and its center is 3 mm from the skin surface. Figure 4e shows the simulated central temperature (T_c) of biological tissues as a function of different thermal diffusion depths when using HTPs with different areas, according to 3D modeling. Numerical simulations also show that no excessive heat is exposed to the subcutaneous tissues under $\Delta T = 5.0$ °C. For example, when the area of the HTP is expanded from 0.6×0.6 cm^2 to 3.0×3.0 cm^2, the simulated average tumor temperature increases from 38.2 °C to above 39.7 °C, or even higher. Consequently, this increase in area requires higher power consumption to accommodate, due to the increased heat dissipation area (Figure S24b, Supporting Information). Heat is dissipated by the distal blood flow (Figure 4f). The details of thermal modeling are

© 2022 Wiley-VCH GmbH

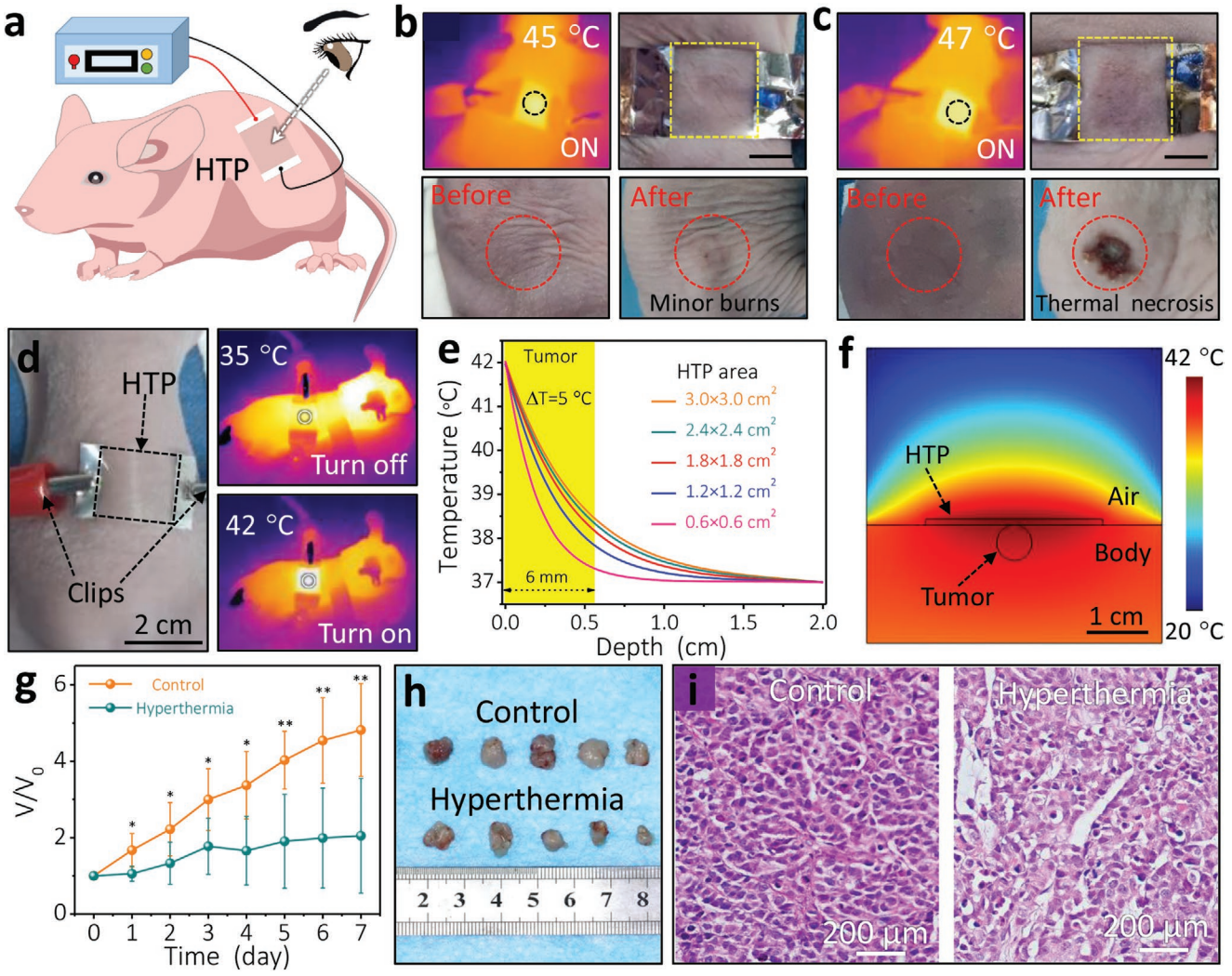

Figure 4. Therapeutic efficacy of the HTP in a tumor-bearing mouse model. a) Schematic illustration of hyperthermia using the HTP for subcutaneous tumors. Comparison of hyperthermia effects for the HTP at two overheating temperatures of b) 45, and c) 47 °C. Scale bars: 1 cm. d) Images of mild-thermic tumor treatments: optical (left), IR images before (top) and during (bottom) hyperthermia while the HTP was attached. e) Simulated temperature profiles of the HTPs with different areas from the skin surface into subcutaneous tissue at a given temperature (42.0 °C). The shadowed part represents the area where the tumor is located. f) Contour map of the temperature distribution during hyperthermia. g) Tumor volume growth curves for the orthotopic tumor models (n = 6 biologically independent samples). (h) Representative photographs of the dissected tumors. i) H&E staining images of tumor tissue sections.

provided in the Methods section. As shown in Figure 4g, the hyperthermia groups (received mild-thermic treatment for 7 days) revealed significant tumor growth inhibition (two-fold), compared to the control groups (without any treatment). The tumors in the hyperthermia groups had the minimum volumes (Figure 4h), which were in accordance with the change of the tumor weights (Figure S26a, Supporting Information). Hematoxylin and eosin (H&E) staining images displayed that tumor tissues indicate obvious apoptosis/necrosis after hyperthermia, which was characterized by a decrease in the number and size of the cells, as well as a decrease in nucleoplasmic concentration (Figure 4i). Also, no pathological damage or inflammation could be found among the groups in representative H&E staining results from the main organs (Figure S27, Supporting Information), indicating the mild-thermic treatment with HTPs is a highly safe treatment option. Meanwhile, all the mice in hyperthermia groups did not show body weight loss. During the hyperthermia, the tumor-bearing mice also had no effect on water/food intake (Figure S26b–d, Supporting Information). These body therapeutic results fully prove that the transparent HTP, which operates based on Joule heating, is a promising route for treating some superficial tumors, such as breast cancer and skin cancer.

2.5. Mechanism Analysis of Tumor Thermal Ablation

To explore the possible existing mechanisms of tumor thermal ablation, the expression of target molecules related to apoptotic signaling pathways was investigated. The tumors were

© 2022 Wiley-VCH GmbH

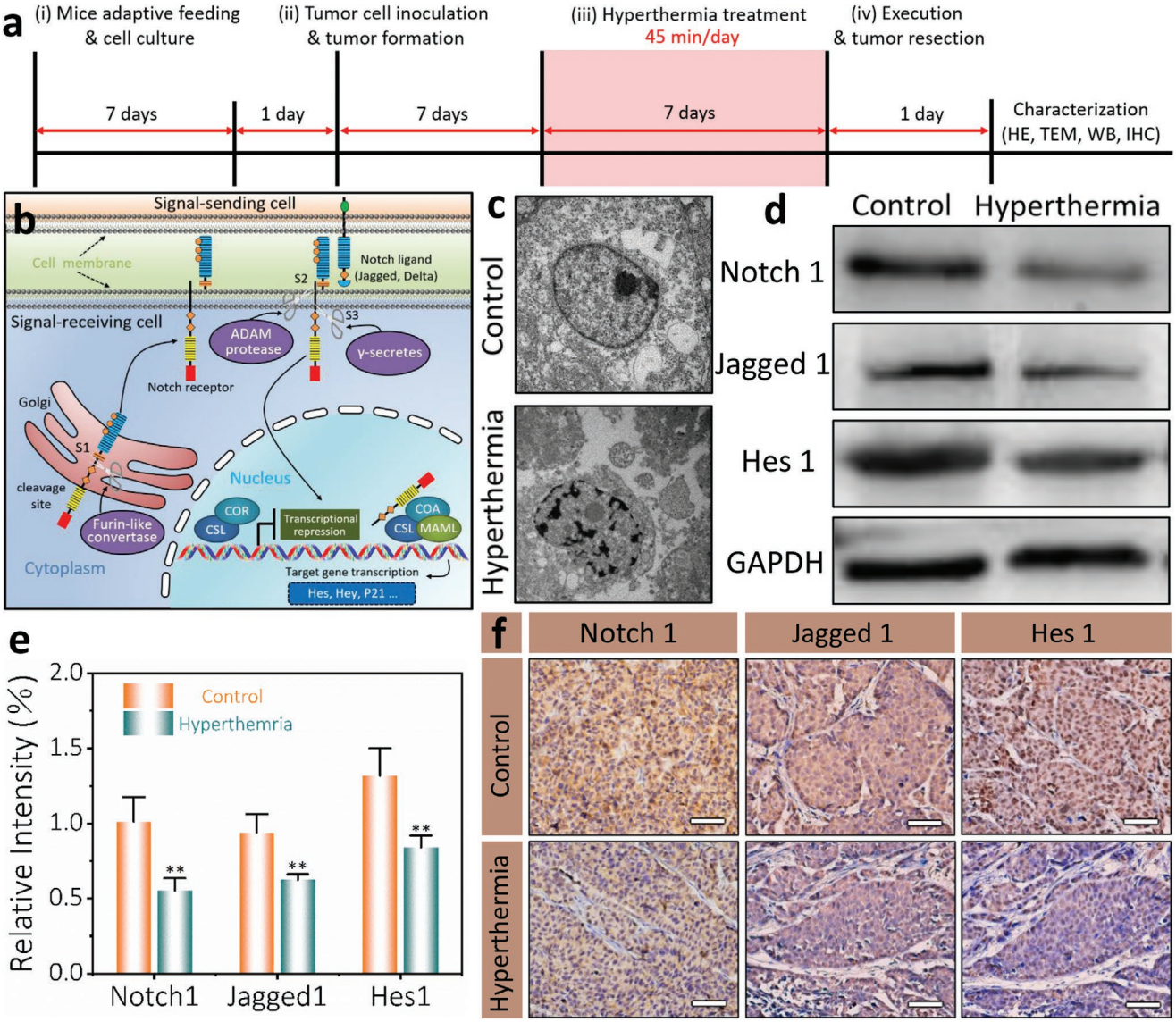

Figure 5. Underlying mechanisms of hyperthermia-induced apoptosis. a) Detailed treatment plan used to investigate the HTP in mouse model. b) Illustration of the Notch signaling pathway. See main text for details. c) Representative TEM images showing morphological changes of CAL-27 cells. d) Representative WB images showing changes of apoptosis-related proteins, and e) corresponding quantitative analysis. f) Representative results of IHC. Brown and blue represent positive and negative expressions, respectively. Scale bars: 200 μm.

collected and characterized after hyperthermia. The detailed mild-thermic treatment procedure is presented in **Figure 5**a. In recent years, a growing number of studies have shown that the abnormal activation of Notch receptors is related to the tumor metabolic/apoptotic processes.[46–47] The Notch signaling pathway includes four parts: the Notch receptor and its ligand, DNA binding sequence CSL (CBF1/Suppressor of hairless/Lag-1), and other effectors/Notch regulators. There are four subtypes of Notch receptors and five Notch ligands (including Delta-like, and Jagged) in mammals. As illustrated in Figure 5b, the typical Notch signaling pathway involves a three-step proteolytic cleavage, leading to the Notch intracellular domain (NICD) to be released into the cytoplasm. Then the NICD enters the nucleus and combines with the CSL transcription factor to form the NICD/CSL transcriptional activation complex, which activates the downstream target genes such as HES and HEY. Different roles of the Notch signaling pathway in cancer depend on the cell type and microenvironment and may be either carcinogenic or tumor-suppressive.[47] Some researchers have studied the role of the Notch signaling pathway in the proliferation and apoptosis of human tongue squamous cell carcinoma, and the results showed that the inhibition of the Notch1 receptor can significantly inhibit proliferation and induce apoptosis of tongue squamous cell carcinoma. Those results indicate that the Notch signaling pathway is actively expressed in human tongue squamous cell carcinoma, and its abnormal activation can promote the proliferation and induce the apoptosis of tongue squamous cell carcinoma.[48]

© 2022 Wiley-VCH GmbH

Therefore, in this study, we investigated whether hyperthermia can induce the apoptosis of tongue squamous cell carcinoma cells by inhibiting the expression of Notch signaling molecules. The morphological changes of tumor cells treated with hyperthermia were observed using transmission electron microscopy (TEM). As shown in Figure 5c, the hyperthermia-treated cell nucleus was cracked into many fragments, resulting in apoptotic bodies, and the organelle structure and cell membrane were destroyed. Subsequently, the measured Western blot (WB) results (Figure 5d) from the hyperthermia group exhibited downregulated expression of Notch 1, Jagged 1, and Hes 1 proteins, compared with the control group. There was no significant difference in GAPDH protein expression between the two groups. The corresponding WB quantitative analysis using ImageJ software was plotted in Figure 5e. Furthermore, the corresponding immunohistochemical (IHC) analysis also supports this point (Figure 5f). These results collectively corroborate hyperthermia can significantly inhibit the growth of subcutaneous tumors by inducing cell apoptosis, and the Notch signaling pathway plays an important role in it.

3. Conclusion

In conclusion, this work demonstrates an unusual, soft HTP that features broad-spectrum transparency, rapid-response, uniform-temperature distribution, reusability, and ultra-low voltage operation to address the need in subcutaneous tumor treatment. Unlike traditional transparent heating components based on mesh-like percolating structures, each of the ultralong unidirectional AgNFs within the HTP acts as an independent conducting path, which is not affected by percolation, achieving both high transparency, low electrical resistivity and excellent electrothermal performances. The HTP can be used in various conditions, such as repeated bending and in high and low ambient temperatures, while also remaining conformally attached to dynamically curved surfaces (e.g., human joints). Its hyperthermia capabilities have been confirmed in mice with tumors under the skin. High transparency allows the observation of the treatment effect in real-time, in a closed-loop fashion. The HTP is also light-transmissive in the near UV and IR ranges, allowing it to be directly UV sterilized. To further improve the safety and precision of the device, a closed-loop temperature monitoring and temperature control can be further achieved by integrating temperature sensors or tracking with real-time temperature readers. The HTP reported here offers a safe, non-invasive, mild-thermic treatment route for superficial tumors that can overcome the deficiencies of traditional tumor treatment therapies. In particular, for patients with advanced tumors that have recurred after radiotherapy, chemotherapy, or surgery, and cannot continue to receive the aforementioned treatments, our HTP can be used as a palliative treatment to alleviate the intractable pain caused by advanced tumors and improve the quality of life. Such a device also holds great promise in treating many other diseases, such as osteoarthritis, cervical spondylosis, and chronic ocular surface inflammation. Besides therapy and treatment, the HTP can serve as a critical and effective device to facilitate medical diagnostics, such as pulse oximetry.

4. Experimental Section

Preparation of AgNFs Network in Different Directions: The freestanding AgNFs network was prepared through electrospinning combined with magnetron sputtering. PVA powder (average molecular weight, 75 000, Sigma-Aldrich) was dissolved into deionized (DI) water at a concentration of 10 wt%, and then stirred for about 2 h at 80.0 °C. The operating voltage, collector distance (between the needle and the grounded metal collectors), and flow rate were set to 15 kV, 15 cm, and 2.0 mL h^{-1}, respectively. Direction of PVA nanofibers was controlled by changing the metal collectors in the electrospinning process. The desired PVA nanofibers were collected on a custom-made double-side metal frame. The resulting unidirectional PVA nanofibers network was dried at room temperature for 24 h. Subsequently, a thin layer of Ag with the thickness of ≈60 nm was covered onto PVA nanofibers using direct current sputtering with a power of 4 W in Ar ambience, forming a uniform conformal coating with the core–shell structure. In contrast, omnidirectional AgNFs network was prepared on a rectangular metal frame.

Fabrication of the HTPs: The preparation process of the HTPs is shown in Figure S1 (Supporting Information). First, the previously prepared PVA aqueous solution (10 wt%) was deposited on polyethylene terephthalate (PET) substrates via a spin-coating method, to serve as a supporting layer. Before using, PET substrates were ultrasonically cleaned for 10 min in acetone, ethanol, and DI water in turn. Then the dried freestanding AgNFs network was attached at a certain angle onto PET substrates coated with PVA film. For the unidirectional AgNFs network, nanofibers arrangement is aligned perpendicular to the electrodes. Due to the random direction of the omnidirectional AgNFs, they can be arranged in any way. Through a patterned shadow mask process, the metallic Ag electrodes were magnetron-sputtered on the two sides of AgNFs network. Finally, polyvinylpyrrolidone (PVP) (average molecular weight, 1 300 000, Sigma-Aldrich) was dissolved in ethanol with 10 wt% at 60 °C. The resulting PVP solution was further spin-coated on the attached unidirectional AgNFs network. After drying, the prepared PVP/AgNFs/PVA film was peeled off from the PET substrates, with a completely external packaging layer using polydimethylsiloxane (PDMS, Sigma-Aldrich). The mass ratio of base to curing agent in the used PDMS used was 10:1. The PDMS-encapsulated HTP was further cured at 80.0 °C for 1 h.

Device Characterization: Morphologies of the samples were observed with a field-emission SEM (FEI-SEM, Apreo S). Real-time resistance was measured using a Keysight 2700 Multimeter. Light transmission spectrum was obtained on a UV-Vis spectrophotometer (U-3900H, HITACHI). The crystal structure of sputtered Ag was obtained by XRD measurement (Philips, X'Pert Pro, Cu Kα radiation; 0.154056 nm). For the Joule heating investigation, constant voltage was applied to the HTPs using a direct current power supply (RD-3030). An infrared radiation thermometer was used to monitor the surface temperature of THPs. An infrared thermal imager (FLIR T460) was utilized to take infrared photos and videos during the heating process. Informed consent was obtained from the volunteer for their participation in the human experiments in this study.

Finite Element Analysis (FEA): The temperature distribution of AgNFs-based HTPs during the heating process was simulated by finite element methods in COMSOL Multiphysics using the heat transfer module. To reduce the computational complexity, the HTP and human tissue were simply modeled as single layer with homogeneous thermophysical properties, with a thermal conductivity of 0.18 W m^{-1} K^{-1} and 0.49 W m^{-1} K^{-1}, a specific heat capacity of 1382 J kg^{-1} K^{-1} and 3421 J kg^{-1} K^{-1}, respectively. The electrical conductivity of the HTPs was calculated using the equation $\sigma = 1/\rho = L/RS$, where ρ is the electrical resistivity, L is the distance between the two electrodes, R is the volume resistance, and S is the cross-sectional area of the specimen. Heating model of HTPs in the air. All free surfaces of HTPs were furnished with convection to static ambient air (12.0 °C) with a convection coefficient of 5.6 W m^{-2} K^{-1}. Hyperthermia model of subcutaneous tumor with HTPs. The lower surface of the human tissue was set to body temperature (37.0 °C), the upper surface was furnished with convection to static ambient air (20.0 °C) with a convection coefficient of 5.6 W m^{-2} K^{-1}, and the remaining surfaces were set to thermal insulation conditions.

© 2022 Wiley-VCH GmbH

Cell Lines and Animal Experiments: Human Cal-27 tongue squamous carcinoma cell line (ATCC, Manassas, VA, USA) was cultured in DMEM that was supplemented with 10% FBS and maintained in a wet environment with 5% CO_2 at 37.0 °C. Male nude BALB/c mice aged 4–5 weeks old (18–22 g) were purchased from Beijing Vital River. Mice were housed in a specific pathogen-free laboratory. The protocol approved by the Ethics Committee of Lanzhou University was followed. The investigation conformed to Lanzhou University animal policies and the Association for Assessment and Accreditation of Laboratory Animal Care accreditation standards under protocol (LZUKQ-2019-044). Cal-27 cells with 2×10^6 were injected subcutaneously into the rear back of nude mice. When the average diameter of subcutaneous tumors reached 5 mm, nude mice were randomly divided into experimental and control groups (6 mice/group). The experimental group received hyperthermia treatment at 42.0 °C for 45 min every day for seven days. The length and width of tumors were measured every day, and the tumor volume was evaluated as volume = (length × width^2 /2). On the second day after hyperthermia, the nude mice were sacrificed by cervical dislocation and the transplanted tumor tissues were removed for subsequent study.

HE Staining Analysis: The transplanted tumor tissue blocks and the tissues of the heart, liver, spleen, lung and kidney of nude mice were fixed with 10% neutral formalin solution, followed by routine paraffin embedding, making slices, and staining with hematoxylin-eosin. After staining, the changes of tumor cell arrangement, cell morphology, nuclear to cytoplasm ratio and other changes, as well as tumor metastasis and morphological changes in various organs of nude mice were observed under a microscope.

TEM Images of Tumor Tissue: The transplanted tumor tissue pieces of nude mice were fixed in 2.5% glutaraldehyde solution, rinsed and dehydrated with graded ethanol, then embedded and polymerized to make ultrathin sections with a thickness of about 55–75 nm. A Tecnai G2 Spirit Bio-twin biological microscope was used to observe the ultrastructure of tumor cells and evaluate the cell apoptosis.

Western Blot Test: Proteins were extracted from the transplanted tumor tissue of nude mice and their concentration was determined. A certain amount of protein samples was taken and subjected to SDS-polyacrylamide gel electrophoresis, film transfer, sealing, primary antibody and secondary antibody incubation, and then exposed in an automatic chemiluminescence apparatus and images were collected. The image analysis was performed using ImageJ software to evaluate the expression of Notch 1, Jagged 1, HES 1, and GAPDH proteins.

IHC (Immunohistochemical): The xenograft tissue of nude mice was fixed with 10% neutral formalin solution. After paraffin embedding, sectioning, dewaxing hydration, antigen repair and peroxidase blocking, the tissue sections were sealed with goat serum and incubated with primary and secondary antibodies. DAB solution was used for color rendering, and the images were observed and photographed under a microscope.

Supporting Information

Supporting Information is available from the Wiley Online Library or from the author.

Acknowledgements

Q.W., H.S., and Y.L. contributed equally to this work. This work was supported by the National Natural Science Foundation of China (Nos. 61874166 and U1832149 to W.L.), the Science and Technology Program of Qinghai Province (No. 2020-HZ-809 to W.L.), and the Scientific and Technological Foundation of Gansu Province (No. 20JR10FA670 to J.W.).

Conflict of Interest

The authors declare no conflict of interest.

Data Availability Statement

The data that support the findings of this study are available from the corresponding author upon reasonable request.

Keywords

hyperthermia, silver nanofibers, transparent, tumor treatment, wearable devices

Received: November 5, 2021
Revised: December 18, 2021
Published online: January 17, 2022

[1] N. R. Datta, S. G. Ordonez, U. S. Gaipl, M. M. Paulides, H. Crezee, J. Gellermann, D. Marder, E. Puric, S. Bodis, *Cancer Treat. Rev.* **2015**, *41*, 742.
[2] V. Grégoire, J. L. Lefebvre, L. Licitra, E. Felip, *Ann. Oncol.* **2010**, *21*, v184.
[3] R. Vaish, S. Gupta, A. K. D'Cruz, *N. Engl. J. Med.* **2015**, *373*, 2477.
[4] M. Nagata, H. Nakayama, T. Tanaka, R. Yoshida, Y. Yoshitake, D. Fukuma, K. Kawahara, Y. Nakagawa, K. Ota, A. Hiraki, M. Shinohara, *Br. J. Cancer* **2011**, *105*, 1322.
[5] B. Solomon, R. J. Young, D. Rischin, *Semin. Cancer Biol.* **2018**, *52*, 228.
[6] T. J. Dougherty, C. J. Gomer, B. W. Henderson, G. Jori, D. Kessel, M. Korbelik, J. Moan, Q. Peng, *J. Natl. Cancer Inst.* **1998**, *90*, 889.
[7] W. Lan, Y. Chen, Z. Yang, W. Han, J. Zhou, Y. Zhang, J. Wang, G. Tang, Y. Wei, W. Dou, Q. Su, E. Xie, *ACS Appl. Mater. Interfaces* **2017**, *9*, 6644.
[8] S. Michlovitz, L. Hun, G. N. Erasala, D. A. Hengehold, K. W. Weingand, *Arch. Phys. Med. Rehabil.* **2004**, *85*, 1409.
[9] J. S. Petrofsky, M. Laymon, H. Lee, *Med. Sci. Monit.* **2013**, *19*, 661.
[10] S. Michlovitz, L. Hun, G. N. Erasala, D. A. Hengehold, K. W. Weingand, *Arch. Phys. Med. Rehabil.* **2004**, *85*, 1409.
[11] S. Choi, J. Park, W. Hyun, J. Kim, J. Kim, Y. B. Lee, C. Song, H. J. Hwang, J. H. Kim, T. Hyeon, D.-H. Kim, *ACS Nano* **2015**, *9*, 6626.
[12] Z. Ma, S. Kang, J. Ma, L. Shao, A. Wei, C. Liang, J. Gu, B. Yang, D. Dong, L. Wei, Z. Ji, *ACS Nano* **2019**, *13*, 7578.
[13] S. Lee, S. W. Kim, M. Ghidelli, H. S. An, J. Jang, A. L. Bassi, S. Y. Lee, J. U. Park, *Nano Lett.* **2020**, *20*, 4872.
[14] D. T. Papanastasiou, A. Schultheiss, D. Muñoz-Rojas, C. Celle, A. Carella, J.-P. Simonato, D. Bellet, *Adv. Funct. Mater.* **2020**, *30*, 1910225.
[15] J. Jang, J. Kim, H. Shin, Y.-G. Park, B. J. Joo, H. Seo, J.-e. Won, D. W. Kim, C. Y. Lee, H. K. Kim, J.-U. Park, *Sci. Adv.* **2021**, *7*, eabf7194.
[16] J. Kang, H. Kim, K. S. Kim, S. K. Lee, S. Bae, J. H. Ahn, Y. J. Kim, J. B. Choi, B. H. Hong, *Nano Lett.* **2011**, *11*, 5154.
[17] J. Zhi, M. Zhou, Z. Zhang, O. Reiser, F. Huang, *Nat. Commun.* **2021**, *12*, 445.
[18] Y. H. Yoon, J. W. Song, D. Kim, J. Kim, J. K. Park, S. K. Oh, C. S. Han, *Adv. Mater.* **2007**, *19*, 4284.
[19] V. Sharma, A. Koivikko, K. Yiannacou, K. Lahtonen, V. Sariola, *npj Flexible Electron.* **2020**, *4*, 27.
[20] J. Liang, Y. Huang, L. Zhang, Y. Wang, Y. Ma, T. Guo, Y. Chen, *Adv. Funct. Mater.* **2009**, *19*, 2297.
[21] N. Lu, C. Lu, S. Yang, J. Rogers, *Adv. Funct. Mater.* **2012**, *22*, 4044.
[22] D. Han, Y. Li, X. Jiang, W. Zhao, F. Wang, W. Lan, E. Xie, W. Han, *Compos. Sci. Technol.* **2018**, *168*, 460.

© 2022 Wiley-VCH GmbH

[23] P. J. King, T. M. Higgins, S. De, N. Nicoloso, J. N. Coleman, *ACS Nano* **2012**, *6*, 1732.
[24] T. M. Higgins, J. N. Coleman, *ACS Appl. Mater. Interfaces* **2015**, *7*, 16495.
[25] C. Zhang, B. Anasori, A. Seral-Ascaso, S.-H. Park, N. McEvoy, A. Shmeliov, G. S. Duesberg, J. N. Coleman, Y. Gogotsi, V. Nicolosi, *Adv. Mater.* **2017**, *29*, 1702678.
[26] H. Sheng, X. Zhang, Y. Ma, P. Wang, J. Zhou, Q. Su, W. Lan, E. Xie, C. J. Zhang, *ACS Appl. Mater. Interfaces* **2019**, *11*, 8992.
[27] T. J. Kang, T. Kim, S. M. Seo, Y. J. Park, Y. H. Kim, *Carbon* **2011**, *49*, 1087.
[28] C. Celle, C. Mayousse, E. Moreau, H. Basti, A. Carella, J. P. Simonato, *Nano Res.* **2012**, *5*, 427.
[29] T. Kim, Y. W. Kim, H. S. Lee, H. Kim, W. S. Yang, K. S. Suh, *Adv. Funct. Mater.* **2013**, *23*, 1250.
[30] S. Hong, H. Lee, J. Lee, J. Kwon, S. Han, Y. D. Suh, H. Cho, J. Shin, J. Yeo, S. H. Ko, *Adv. Mater.* **2015**, *27*, 4744.
[31] J. Kang, Y. Jang, Y. Kim, S.-H. Cho, J. Suhr, B. H. Hong, J.-B. Choi, D. Byun, *Nanoscale* **2015**, *7*, 6567.
[32] A. Y. Kim, M. K. Kim, C. Hudaya, J. H. Park, D. Byun, J. C. Lim, J. K. Lee, *Nanoscale* **2016**, *8*, 3307.
[33] Y. Li, Z. Zhang, X. Li, J. Zhang, H. Lou, X. Shi, X. Cheng, H. Peng, *J. Mater. Chem. C* **2017**, *5*, 41.
[34] D. Lordan, M. Burke, M. Manning, A. Martin, A. Amann, D. O'Connell, R. Murphy, C. Lyons, A. J. Quinn, *ACS Appl. Mater. Interfaces* **2017**, *9*, 4932.
[35] J. Bustillos, C. Zhang, B. Boesl, A. Agarwal, *ACS Appl. Mater. Interfaces* **2018**, *10*, 5022.
[36] L. Li, S. K. Hong, Y. Jo, M. Tian, C. Y. Woo, S. H. Kim, J. M. Kim, H. W. Lee, *ACS Appl. Mater. Interfaces* **2019**, *11*, 16223.
[37] Q. Liu, B. Tian, C. Luo, J. Liang, W. Wu, *Adv. Mater. Technol.* **2020**, *5*, 2000278.
[38] F. Wang, W. Wang, X. Mu, J. Mao, *Chem. Eng. J.* **2020**, *395*, 125183.
[39] A. J. Hartz, M. E. Fischer, G. Bril, S. Kelber, D. Rupley, B. Oken, A. A. Rimm, *J. Chronic Dis.* **1986**, *39*, 311.
[40] D. T. Felson, A. Naimark, J. Anderson, L. Kazis, W. Castelli, R. F. Meenan, *Arthritis Rheum.* **1987**, *30*, 914.
[41] W. M. Schramm, A. Bartunek, H. Gilly, *Int. J. Clin. Monit. Comput.* **1997**, *14*, 17.
[42] K. Budidha, P. A. Kyriacou, 2015 37th *Annual Int. Conf. of the IEEE Engineering in Medicine and Biology Society*, IEEE, Piscataway, NJ **2015**.
[43] K. A. Takahashi, H. Tonomura, Y. Arai, R. Terauchi, K. Honjo, N. Hiraoka, T. Hojo, T. Kunitomo, T. Kubo, *Int. J. Hyperthermia* **2009**, *25*, 661.
[44] K. Takahashi, T. Suyama, Y. Takakura, S. Hirabayashi, N. Tsuzuki, Z.-S. Li, *J. Phys. Therapy Sci.* **2000**, *12*, 43.
[45] H. Xiang, L. Zhao, L. Yu, H. Chen, C. Wei, Y. Chen, Y. Zhao, *Nat. Commun.* **2021**, *12*, 218.
[46] O. Meurette, P. Mehlen, *Cancer Cell* **2018**, *34*, 536.
[47] J. C. Aster, W. S. Pear, S. C. Blacklow, *Annu. Rev. Pathol.* **2017**, *12*, 245.
[48] T. H. Zhang, H. C. Liu, G. Q. Liao, *Oral Oncol.* **2011**, *47*, S123.

© 2022 Wiley-VCH GmbH